Cliff coast collapses driven by nested biological, astronomical and meteorological activity cycles

Michael Dietze, GFZ German Research Centre for Geosciences, Section 4.6 Geomorphology, Potsdam, Germany (mdietze@gfz-potsdam.de),

Kristen L. Cook, GFZ German Research Centre for Geosciences, Section 4.6 Geomorphology, Potsdam, Germany (klcook@gfz-potsdam.de),

Luc Illien, GFZ German Research Centre for Geosciences, Section 4.6 Geomorphology, Potsdam, Germany (lillien@gfz-potsdam.de),

Oliver Rach, GFZ German Research Centre for Geosciences, Section 4.6 Geomorphology, Potsdam, Germany (racho@gfz-potsdam.de),

Stephanie Puffpaff, National Park Authority Vorpommern, Research and Monitoring Division, Jasmund, Germany (s.puffpaff@npa-vp.mvnet.de)

Ingolf Stodian, National Park Authority Vorpommern, Research and Monitoring Division, Jasmund, Germany (i.stodian@npa-vp.mvnet.de)

Niels Hovius, GFZ German Research Centre for Geosciences, Section 4.6 Geomorphology, Potsdam, Germany (hovius@gfz-potsdam.de),

Abstract

Direct links between cliff erosion and forcing mechanisms are poorly constrained, largely due to the difficultly of obtaining precise timing information for individual failure events. Here we use two years of seismic records and auxiliary data to precisely detect and locate 81 failure events at the chalk cliff coast of Germany's largest island, Rügen. The sub-second timing precision allows the linking of individual events to triggers over a wide range of relevant time scales. We show that in the monitoring interval, marine processes were negligible and cliff failure was associated with terrestrial controls on moisture. Failures were mostly triggered when water caused a state transition from solid to liquid. Water content can be changed by i) subsurface flow towards the cliff, ii) rain onto the cliff and iii) condensation of air moisture, leading to clustered events during night time. Failure periodicity is in alignment with the lunar cycle. Seasonal water availability, controlled by plant activity, sets cliff dynamics at the annual scale. Wetter and drier than average years impose a month-long legacy effect for cliff dynamics.

This paper is a non-peer reviewed preprint uploaded to EarthArXiv, and submitted to "Journal of Geophysical Research: Earth Surface". This is the first submitted version of the manuscript.

Potsdam, 12 December 2019

Cliff coast collapses driven by nested biological, astronomical and meteorological activity cycles

M. Dietze[1], K. L. Cook[1], L. Illien[1], O. Rach[1], S. Puffpaff[2], I. Stodian[2], N. Hovius[1]

[1]GFZ German Research Centre for Geosciences, Section 4.6 Geomorphology, Potsdam, Germany
[2]National Park Authority Vorpommern, Research and Monitoring Division, Jasmund, Germany

Key Points:

- UAV and seismically detected cliff coast failures are forced on diurnal, lunar, seasonal and multi-year scale
- Failures are controlled by water availability, provided by groundwater, condensation of air humidity, and rain on the cliff
- Short term activity patterns are modulated by biota activity and the water budget inherited from the previous season

Corresponding author: Michael Dietze, `mdietze@gfz-potsdam.de`

Abstract

Direct links between cliff erosion and forcing mechanisms are poorly constrained, largely due to the difficultly of obtaining precise timing information for individual failure events. Here we use two years of seismic records and auxiliary data to precisely detect and locate 81 failure events at the chalk cliff coast of Germany's largest island, Rügen. The sub-second timing precision allows the linking of individual events to triggers over a wide range of relevant time scales. We show that in the monitoring interval, marine processes were negligible and cliff failure was associated with terrestrial controls on moisture. Failures were mostly triggered when water caused a state transition from solid to liquid. Water content can be changed by i) subsurface flow towards the cliff, ii) rain onto the cliff and iii) condensation of air moisture, leading to clustered events during night time. Failure periodicity is in alignment with the lunar cycle. Seasonal water availability, controlled by plant activity, sets cliff dynamics at the annual scale. Wetter and drier than average years impose a month-long legacy effect for cliff dynamics.

Plain Language Summary

Cliffs line many coastlines and tend to fail catastrophically, mobilizing large volumes of material. This has consequences for human safety, ecosystems and availability of sediment along the coast. The time gap between fast failure processes and oft used episodic observation techniques does not allow a full analysis of the drivers and causes of cliff erosion. By combining measurements of a seismometer network on Germany's largest island Rügen with 3D models from drone surveys and weather station data we studied 81 cliff failure events in two years. These events are predominantly caused by water availability, which turns the solid cliff building chalk into a slurry prone to failure. Water availability is modulated at different scales by rain on the cliff and air moisture condensation, soil water flow, vegetation water uptake, and planetary gravity. Our findings sharpen the picture of when and why cliffs fail, and allow a better understanding of future global change impact on cliff coasts.

1 Introduction

Coasts host about 40 % of the world's global population along with key infrastructure, cultural heritage and unique ecosystems (Menatschi et al., 2018). Coastal change can have a profound impact on these assets. Around half of the world's coasts consist of eroding cliffs (Young & Carilli, 2019) and cliff failure across a range of scales is a fundamental mechanism of coastal retreat. Cliff failure is driven by cyclic loading and agitation by climate-driven processes. These include impact of tide- and storm-driven waves that exert forces on the cliff and entrain abrasive sediment (Stephensen, 2014), wind-induced stress (Vann Jones et al., 2015), amplified when interacting with trees (Dietze, Turowski, et al., 2017), frost shattering or ice segregation and freeze thaw cycles (Letortu et al., 2015), and rainfall and groundwater recharge that lead to gravitational loading, reduced shear strength, increased pore water pressure, and lubrication of discontinuities (Stephensen, 2014), among others (cf. Dietze, Turowski, et al., 2017).

Robust attribution of cliff failure to a particular trigger depends on precise knowledge of the timing and location of the event and of the ambient conditions prior to and during the event. Because failure is a fast process that can potentially happen along an entire coast stretch, and relevant conditions can change on short time scales (minutes to days), data with at least hourly resolution is required to constrain causal links. Many studies have used records of cliff failure with monthly or coarser time resolution (e.g. Lim et al., 2010; Vann Jones et al., 2015). While these studies have yielded many useful insights, we suggest that environmental seismology has the potential to give more detailed understanding of links between cliff failure and its drivers.

Networks of seismic sensors can be used to detect, locate, and estimate the volume and anatomy of mass movement events at the landscape scale (e.g. Helmstetter & Garambois, 2010; Hibert et al., 2011). The limit of detection for a given network is set by the ambient noise level, and depends on the energy of a mass movement transferred into the substrate, as well as ground properties that determine the propagation and attenuation of the resulting seismic waves. Dietze, Mohadjer, et al. (2017) were able to detect rockfall volumes as small as 0.05 m^3 released at less than 50 m cliff height with seismic location deviations of about 80 m on average (7 % of the mean station spacing). The main strength of this approach, however, is the continuous temporal coverage of a larger area and very precise time information about the onset and duration of single events. This precise time information is key to constraining possible triggers of failure events by measuring the time lag between a trigger and a subsequent geomorphic event (Dietze, Turowski, et al., 2017).

In this article we explore the drivers and triggers of coast cliff failures on Germany's largest island, Rügen. We use seismic and UAV monitoring to detect, date, locate, verify and quantify cliff failures over a period of two years. We analyze the spatial and temporal patterns of cliff failure in the context of marine, meteorological, biological and hydrological boundary conditions across scales from minutes to years. This yields quantitative constraints on the relevance of triggers and drivers at distinct time scales.

2 Materials and methods

2.1 Study site and instrumentation

The Jasmund peninsula on Rügen, where our study is located, comprises weakly cemented Maastrichtian chalk, which has been folded and thrusted by the Scandinavian ice sheet into a sequence of stacked blocks and covered by till. This sequence is exposed along an 8.6 km long stretch of coast containing cliffs that are steep (57^{+8}_{-4} °, median and quartiles) to partly overhanging and up to 118 m high (48^{+13}_{-13} m). The cliffs retreat by erosion at about 25 cm/yr on average, generating 103000 m^3 of debris along the coast section (Obst & Schütze, 2005). This estimate is based on Holocene time scale evidence and allows for significant short-term variability.

From March 2017 to April 2019, we operated four seismic stations (Nanometrics TC 120s seismometers and PE6/B 4.5 Hz geophones, logged at 200 Hz by Digos DataCubes) at intervals of about 1.2 km along the cliff coast. Repeat UAV surveys covered most of the cliff and were used to generate high resolution 3D point clouds to quantify topographic changes. In addition, we used weather data at hourly resolution from the Arkona station of the Deutscher Wetterdienst, 20 km to the northwest (DWD, 2019), sea level data with minute resolution from the southern limit of the study area (WSV, 2019), and daily groundwater data (STALUVP, 2019) from a well 1.5 km west of the cliff coast (Fig. 1).

2.2 Data processing

Seismic data were processed with the R package 'eseis' v. 0.5.0 (Dietze (2018a, 2018b)). Typical seismic waveforms of cliff failures are spindle shaped (Hibert et al., 2011), and are supposed to be recorded with a few seconds offset across the network (Fig. 2 f). To identify these discrete events in the continuous stream of seismic data, we used a STA-LTA picker (Allen, 1982). For details on the settings and parameter constraints see SI. We screened these events with a series of automatic rejection criteria, admitting only events that lasted between 1 and 180 s (assuming that shorter events are random signal coincidences and longer signals are caused by earthquakes or anthropogenic activity). Events needed to be detected by at least three seismic stations (minimum required to locate an event), and must have been registered across the network within 11 s (maximum time

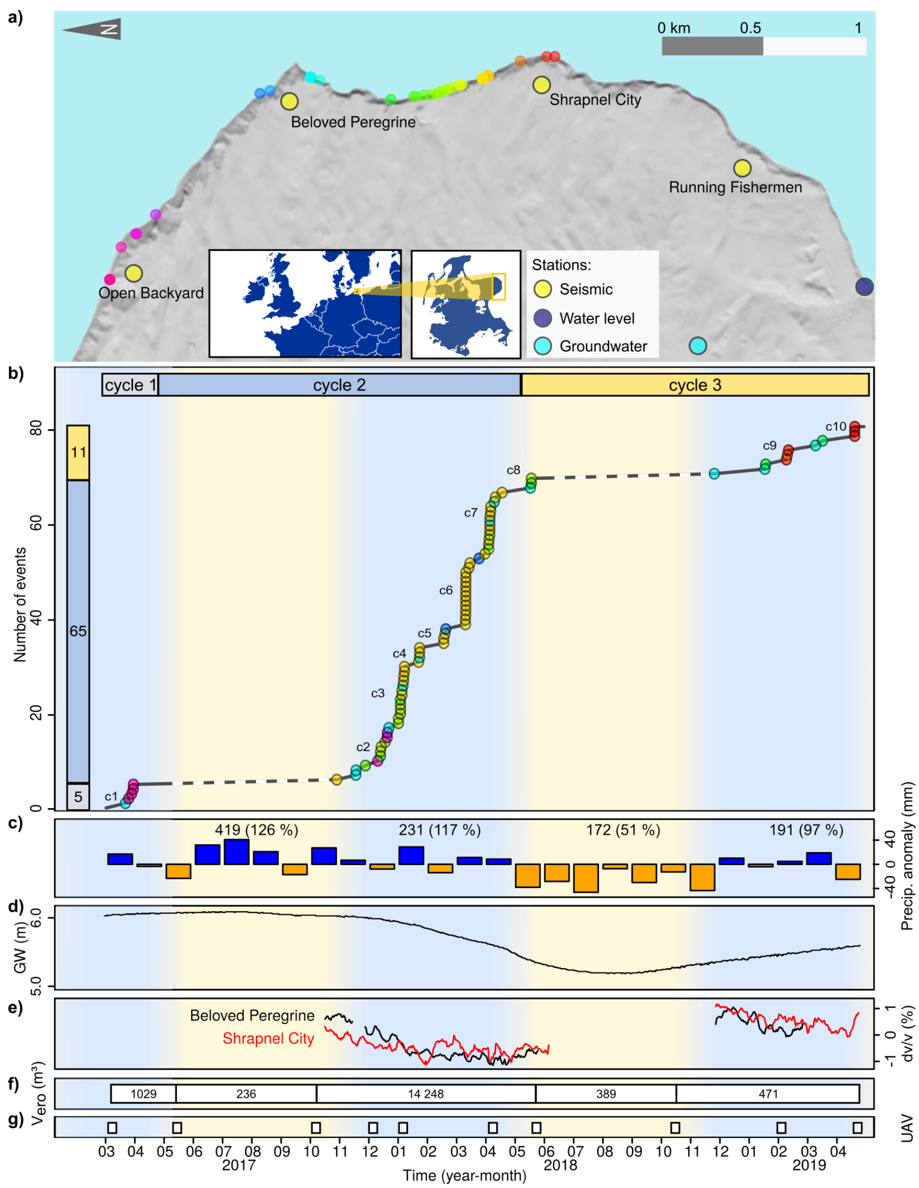

Figure 1. Study area and data sets. a) Hillshade map of study site with seismically detected failure events (coloured by location). b) Failure events with numbered event clusters. Circle colour corresponds to locations in a). Dashed lines show no data periods. c) Bars show precipitation deviations from 30 year averages, DWD (2019). Numbers denote precipitation sums per season. Values in parentheses denote relative deviations from 30 year averages. d) Groundwater level (STALUVP, 2019) above 118 m asl. e) Seismic wave velocity changes (dv/v). f) UAV based failure volume sums per season. g) UAV flight dates.

required for a seismic signal to travel through the network). All admitted events were checked manually for plausibility based on i) consistent amplitude decrease of the signals across the network as expected for a local seismic source, ii) consistent signal arrival time delay across the network, also indicative of a local source predominantly emitting surface waves, iii) an emergent onset and slow decay of the signal, as reported for many hillslope mass wasting processes (Helmstetter & Garambois, 2010; Hibert et al., 2011; Dietze, Mohadjer, et al., 2017), iv) absence of earthquake-like distinct arrivals of different wave types, and v) absence of tremor-like frequency patterns, typical for aircraft. Validated events that passed manual screening were located by migration of the deconvolved, filtered vertical component signal envelopes (Burtin et al., 2013). See SI for details on parameter setup. The final location estimates are reported as projections along the coast, for events whose 90% confidence interval overlapped with the coast as the only likely area of active mass wasting in the otherwise gently undulating landscape. All detailed processing steps are described in the SI, including annotated R scripts.

Seismic noise cross correlation analysis can be used to infer changes in the relative seismic wave velocity (dv/v), a proxy for changes in the properties of the substrate through which random seismic waves travel. We determined dv/v for the two central stations ("Beloved Peregrine" and "Shrapnel City") with the MIIC package (Sens-Schönfelder, 2014). Hourly signals were processed by filtering (4–8 Hz), spectral whitening, clipping at two standard deviations and sign-normalization, and the cross correlation functions were stacked to daily data. These results were converted to dv/v values using the stretching technique of Sens-Schönfelder and Wegler (2006). For details see SI.

UAV surveys were used to verify the seismic event detections and locations, to provide precise locations along the cliff, detachment heights above the shore line and below the cliff top, and to estimate the volumes of failed material. Surveys (Fig. 1 g) were performed using consumer-grade DJI UAVs, including a Phantom 3 Advanced (March 2017, May 2017, Dec. 2017), a Mavic Pro (Oct. 2017, Jan. 2018, April 2018, May 2018), and a Mavic 2 Pro (Nov. 2018, Feb. 2019, April 2019). Each survey consisted of multiple flights from up to seven locations along the cliff, yielding 1000-2000 photos for a full survey. The Dec. 2017, Jan. 2018 and April 2018 surveys were partial surveys, covering the most active cliff sections. The UAVs were flown manually and set to take photographs every three seconds. For a given survey, each section of the cliff was covered by at least two passes of the UAV with different flight elevation and camera obliquity. Camera angles typically ranged from 40–80 degrees from nadir, and elevations from 30–150 m above sea level. The distance between the camera and cliff varied widely depending on cliff height and weather conditions.

UAV data processing was done using Agisoft Photoscan (v. 1.4.2) structure from motion (SfM) software. The cliff was split into five overlapping segments in order to reduce processing time. Because we were unable to deploy or measure ground control points for the cliff surveys, the surveys were georeferenced using only the GPS data recorded by the UAVs. In order to obtain reliable change detection results, we followed to co-alignment workflow introduced in Cook and Dietze (2019). For each pair of surveys that were compared, we combined photos from both surveys for point matching, initial bundle adjustment, and optimization (following removal of tie points with reconstruction uncertainty > 50). The two sets of photos were then separated for the dense cloud construction. Parameters for alignment were: high quality, key point limit of 40000, tie point limit of 4000, and adaptive camera model fitting. Parameters for dense cloud construction were: medium quality and aggressive depth filtering. The dense point clouds were compared using the M3C2 algorithm (Lague & Leroux, 2013) in CloudCompare (GPL, 2019) using the parameters: core point spacing 0.25 m, projection diameter 0.5 m, and normal scales 0.5 m to 4.5 m in 1 m steps. The accuracy of the resulting change cloud was assessed using the calculated changes in the stable areas of the cliff (typically the majority of the cliff face). We estimated a level of detection of 10–15 cm or better for our change maps.

We manually inspected each of the change maps in concert with the before and after photographs to identify cliff failures. For each identified failure, we clipped the before and after point clouds to the area of measured change and calculated the volume using the 2.5D volume tool in CloudCompare. We calculated each volume three times using the X, Y, and Z reference planes to determine the most appropriate reference plane to use for a given failure and estimate a relative volume uncertainty of 9.7 % on average. In addition, we measured the elevation of the center of each failure to give the height above the shoreline and the distance from the cliff top.

2.3 Trigger analysis

We focused on precipitation, wind, freeze-thaw transitions, water level and wave action (Kennedy et al., 2017; Dietze, Turowski, et al., 2017) as triggers of cliff failures. From the range of possible triggers that cause rock slope failure we can exclude geophysical (earthquake, volcanic eruption; (Hibert et al., 2014)) and mass wasting (snow/rock avalanches, icefalls, debris flows; (Stock et al., 2013)) triggers due to the location of the study site. Biological/anthropogenic triggers (animal traffic, human activities; (Wieczorek, 1996)) are unlikely in a protected area with virtually no access to the cliff face. Thermal dilation and contraction (Stock et al., 2013) are unlikely to impose significant stress given the eastern exposure of the cliff where little sunlight reaches the cliff, especially during winter time. The tidal range (Stephensen, 2014) is about 15 cm, equivalent to the diameter of larger sediment clasts on the beach at the foot of the cliff.

We assessed the relevance of the remaining trigger types by analysis of the time difference between an event and the preceding trigger occurrence (Dietze, Turowski, et al., 2017). This assumes that a geomorphic response (i.e., a cliff failure event) occurs while a trigger is active or after it has been active, without delay or with a trigger-specific time lag (cf. Dietze, Mohadjer, et al. (2017) for a detailed discussion of expected time lags). The resolution of any trigger analysis is limited by the resolution and precision of both event timing and trigger proxy data. We are able to reduce the event timing uncertainly to sub-second, rendering trigger proxy time resolution (< 1 h) the limiting factor.

To evaluate the role of precipitation intensity in triggering of cliff failure, we calculated time lags for 0.1 mm/h (smallest measurement increment), 0.2 mm/h ($\text{quantile}_{0.05}$) and 0.5 mm/h ($\text{quantile}_{0.10}$). For wind as trigger we defined wind events as episodes with a one-hour average Beaufort scale 6, labelled "strong wind", or higher. Freeze-thaw episodes were defined as transitions from negative to positive Celsius air temperatures, acknowledging that heat dissipation into the ground can take several hours (Dietze, Mohadjer, et al., 2017) and that there may be differences in air temperature between the study site and the meteorological station. The role of sea level as direct trigger of cliff failures (i.e., minimal time lags) was assessed by calculating time lags for levels corresponding to the $\text{quantiles}_{0.75,0.90,0.95}$ of the full distribution of wave data (i.e., 16, 26 and 33 cm above average sea water level, respectively). In the absence of wave buoy data we cannot directly constrain wave height and therefore assume that high waves coincide with storm events and high water levels. Hence, the wave effect is lumped into the analysis of wind and sea level effects.

The time lags for all triggers are visualised as kernel density plots. We restrict the analysis to a maximum time lag of 72 h under the assumption that all triggers operate at time scales smaller than three days. To estimate the significance of our analyses we test the time lag distributions resulting from the empiric event catalogue for statistic difference from 1001 synthetic event data sets of the same size as the empiric catalogue. Each synthetic data set is generated by randomly assigning event start times for the entire study period. As test for difference we use the two-sample Kolmogorov-Smirnov test.

The length of the monitoring period (25 months) allows us not only to investigate time lags to triggers but also to identify activity across time scales from diurnal to annual. For these cycles we calculated spectra of the continuous time series of potential triggers and drivers. The discrete distribution of cliff failures was converted to a continuous distribution by calculating a kernel density estimate with hourly resolution and a window size of two days (see SI).

3 Results

3.1 Event detection, location and anatomy

Automatic picking yielded a total of 2818 potential events. After manual screening and location, 81 were confirmed as cliff failures (Fig. 1). We use a failure on 21 March 2017 at 4:38 am UTC time to illustrate the insights from combining the seismic monitoring and UAV surveying (Fig. 2 f–g). This event, located about 200 m south of station "Beloved Peregrine", generated a seismic record with an emergent onset, a rise time of 1.5 s, and a fall time of 7.3 s. Photographs taken 3 days after the event confirmed it as a cliff failure that mobilized around 800 m^3 (park authorities estimate) of material that fragmented during transport and covered the beach as a flow-like deposit (Fig. 2 d). Our UAV-based change model shows released and deposited volumes of 920±50 m^3 and 850±42 m^3, respectively (Fig. 2 g). Seismically detected events (figures in SI A5) lasted $9.0^{+2.9}_{-2.0}$ s, almost exclusively with an emergent onset, signal rise times of $2.8^{+1.5}_{-0.8}$ s and fall times of $6.7^{+2.0}_{-2.0}$ s. The signals had central frequencies of $15.9^{+6.6}_{-4.2}$ Hz. In 26 % of all cases, a failure event was succeeded by at least one other less than 200 m away within 24 hours. We recorded one event cluster composed of 11 discrete events during 10.5 hours, starting on 2018-03-09 16:17:15 UTC (see Tab. SI 3).

Based on UAV-derived 3D models, we measured failure volumes between 1.10 and 4985 m^3. The cumulative detected failure volumes were 236 and 389 m^3 for the summer seasons of 2017 and 2018, respectively. For the winter seasons 2017, 2018 and 2019 the cumulative volumes were 1029 (March to May only), 14248 and 471 m^3 (Fig. 1 f). In many cases the UAV imagery showed that new cliff base deposits are amalgams of multiple failures (Fig. 2 b). Failures initiated at heights of $29.0^{+10.5}_{-16.0}$ m asl. and $24.0^{+3.7}_{-9.0}$ m below the cliff top. Because many failure scars and deposits are the result of multiple events, we do not attempt to constrain the relationship between event seismic amplitude and measured volume.

Screening for precursor activity during 60 minutes before the events revealed random brief pulses of seismic activity at the closest station for only a few cases (e.g., 18-04-09 19:04, 18-03-10 02:50, 18-03-09 23:34, 18-02-15 02:15, 18-01-01 02:17). We did not find a systematic increase in amplitude or decrease in recurrence time of these pulses towards the cliff failure.

3.2 Trigger time lags and activity cycles

We measured the time difference between the 81 recorded cliff failures and the preceding manifestation of a potential trigger, and call this the trigger time lag (Fig. 3 a). Freeze-thaw time lags were considered within a 72-hour window. The time lags of the 20 events that fall within this window peaked around 48 h. Time lags for precipitation showed bimodal distributions for all three threshold values at 0–3 and 16–20 h, applying to between 62 and 67 out of the 81 events depending on the rain rate. Sea level time lags were 0–2 h for all three thresholds, applying to 17–30 events. Time lags for wind showed a plateau between 1 and 10 h and secondary modes at 35–55 h for a total of 71 events. Except for wind, all time lag distributions were significantly different from random (i.e., KS test D values > 0.24 and p values < 0.01, see Fig. SI 6).

At scales beyond event-based time lags, failures showed a tendency to occur during nighttime hours. 50 failures occurred between 8 pm and 8 am, and 31 between 8 am and 8 pm (Fig. 3 b), but this variability is not significantly different from random (D = $0.17^{+0.04}_{-0.02}$, p = $0.18^{+0.16}_{-0.12}$). A diurnal pattern was also observed in air humidity, ranging on average between 75 % and 87 % over a day-night cycle in summer (D = $0.38^{+0.08}_{-0.04}$, $p < 0.07$) and between 82 % and 90 % in winter (D = $0.46^{+0.04}_{-0.04}$, $p < 0.002$). During failure event days air humidity was especially high, between 85 % and 94 % (D = $0.38^{+0.08}_{-0.04}$, $p < 0.07$), with peak values preceding cliff failure by 1–2 hours.

At the monthly scale, failures occurred more frequently when the moon was farther away from the cliff (Fig. 3 c). The lunar distance ranges from 350000 to 410000 km, a 14.4 % difference. Spectral analysis revealed statistically significant periodicity modes between 25 and 29 days for lunar distance, precipitation and cliff failures (Fig. 3 d). The systematic relationship with cliff failure was only violated during the days around the year end 2017/18 (Fig. 3 c, cluster c3 in Fig. 1). That episode, with a total of 12 subsequent failures, seven of them at nearly the same location, was associated with persistent precipitation (31 mm in 7 days, compared to a 30 year monthly average of 46 mm).

Detected failure occurrence was highly seasonal (Fig. 1 b) with events predominantly happening in winter. In contrast, precipitation was stronger in summer than in winter (331 mm versus 250 mm). This trend is reflected in the seismic velocity data (Fig. 1 e) with high dv/v values during summer decreasing with the onset of autumn. However, the pattern was decoupled from the evolution of the groundwater level (Fig. 1 d).

Finally, over the instrumented period we have recorded the imprint of a comparatively wet year with 121 % of the 30-year average precipitation, including 124 % for the summer season (May to November 2017), followed by a drier-than-average year with precipitation totaling 74 % of the 30-year average, including a summer season with only 51 % of the average seasonal rainfall (Fig. 1 c). We have detected 65 cliff failures during the wet year, and only 11 events in the dry year.

4 Discussion

4.1 Spatial patterns of cliff failures

Based on previous seismic rockfall detection work (Dietze, Mohadjer, et al., 2017) and our seismic records of tree felling (< 10 t weight and < 15 m fall height) at known locations at least 2.5 km from the instruments in the Rügen study area (see SI for details), we conservatively defined the limit of seismic detection at 4 m^3 of rockfall volume. Any geometric bias in event detection due to the seismic network layout was minimal for the central part of the cliff section, where the distance to a set of three stations in less than two km throughout. Note however that this bias only potentially affects the location, not the detection limit. The size of our catalogue was small compared to catalogues from other approaches (e.g. Lim et al., 2010; Vann Jones et al., 2015). Our data did not allow for meaningful construction of magnitude-frequency relationships and the role of small events (<4 m^3) in long-term cliff erosion, and we did not attempt a full erosional budget. However, the catalogue did allow analysis of activity patterns along the entire cliff coast and investigation of the kinetics of single events, temporal clustering of cliff failures and the links between failures and trigger mechanisms.

Recorded events had similar rise and fall times, durations and frequency contents of seismic signals. Combined with the UAV based locations at $29.0^{+10.5}_{-16.0}$ m above the cliff base and $24.0^{+3.7}_{-9.0}$ m below the cliff top, this suggests that the events had comparable detachment and evolution processes. Predominantly spindle shaped seismograms rather than single seismic pulses, indicative for impacts of an intact volume of rock, may reflect the avalanching movement of fragmented chalk volumes (Hibert et al., 2011; Dietze, Turowski, et al., 2017).

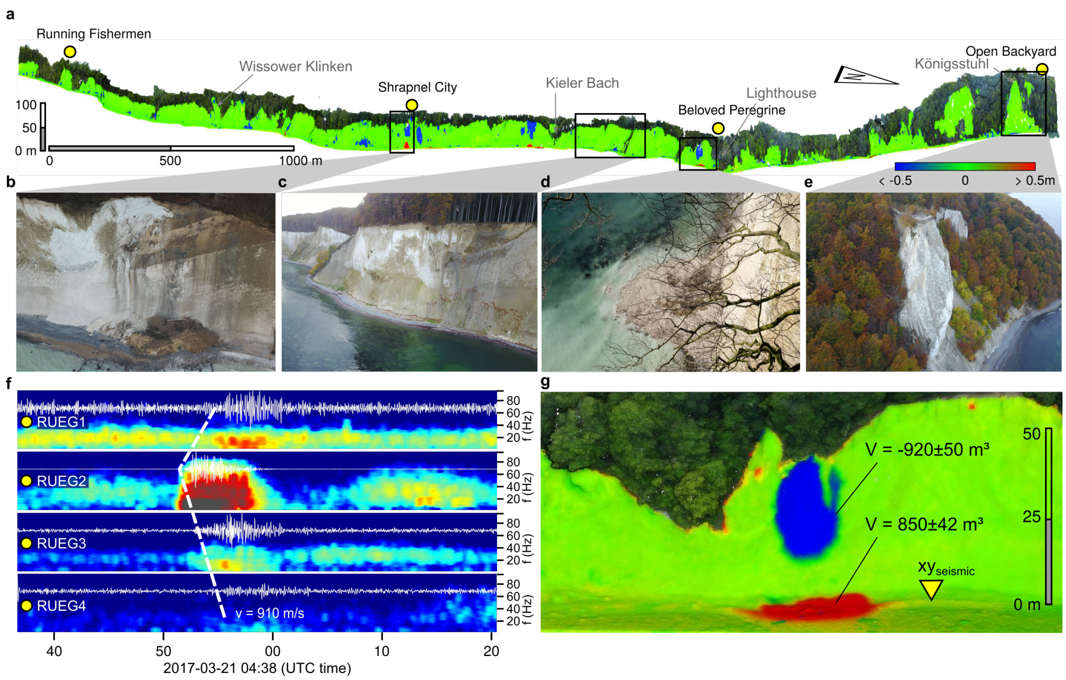

Figure 2. Cliff failure locations, anatomy and deposits. a) UAV-based cliff activity, perspective view from the sea. Tree carapace is shown in natural colour. Colour bar indicates surface change in m. b–e) Characteristic cliff sections and failure types. f) Failure from d) as recorded by the seismic stations with an apparent wave velocity of 910 m/s. The 5–10 Hz filtered signals are plotted on top of spectrograms (scaled between -160 and -100 $(m^2/s^2)/Hz$). g) UAV-based volume changes for the failure in d). Perspective from the sea. Yellow triangle depicts best match seismic location, about 37 m north of the UAV based location.

During the entire survey period, recorded activity was focused in the central cliff section, between stations "Beloved Peregrine" and "Shrapnel City", with only 7 out of 81 outside this reach (Fig. 1). This activity pattern is also expressed in the shape of the different cliff sections. Between the two central stations, the cliff is steepest (46±16 ° average slope), and has the most overhanging facets. It is mostly devoid of vegetation, and has waterfalls at the outlets of creeks. North and south of the two central stations, slopes are gentler, 38±13 ° and 41±16 °, respectively, and several channels have incised to sea level. This contrast suggests that activity segmentation is persistent on geomorphologically significant time scales, with failure-driven cliff retreat in the centre and diffusive or catchment-confined hillslope sediment transport to the north and south.

4.2 Triggers of cliff failures

Cliff failures were significantly linked with precipitation in about half of the cases. Time lags show two clusters, at 0–3 ($n = 19$) and 16–20 ($n = 20$) hours (Fig. 3 a). This suggests that rain may impact the cliff through two different mechanisms. We interpret the rapid response as the effect of rain directly onto the cliff face and the delayed response as the consequence of water flow towards the cliff face within the soil covering the chalk. Typical hydraulic conductivity values for Rügen chalk, kf $\sim 10^{-10}$ m/s (Krienke & Koepke, 2006), allow flow rates of only a few micrometres per day, whereas the higher conductivity of the cover material, kf $\sim 10^{-4}$ m/s, permits water from up to 8.6 m hinterland to seep into the cliff face within a day. Seepage can have a longer range where preferential, lateral flow paths are present.

We reject wind, sea level, waves, and freeze-thaw transitions as triggers based on KS test results (Fig. SI 6) and a lack of plausible mechanisms for the measured time lags. Wind time lags plateau between 0–10 h (Fig. 3 a) and within this are not distinct from random. We do not see any plausible mechanistic interpretation of this distribution. Sea level time lags of 0–3 hours (for 17–30 out of 81 events) are an effect of the seasonally changing water level (514 cm in winter versus 502 cm in summer), which results in winter cliff failures mapping onto high water levels. Tides of $\tilde{1}5$ cm appear to be irrelevant given that the ramp of the shore platform has a height range of 1–2 m. Moreover, the persistence of fine-grained deposits at the cliff base further indicates that waves only rarely impact the base of the cliff. In addition, most of the failures occur at $29.0^{+10.5}_{-16.0}$ m above the beach with no indications of undermining at the base. Thus, we reject high sea levels and tides as trigger mechanisms. Freeze-thaw time lags of about two days (Fig. 3 a) render this mechanism unlikely as well because heat dissipation probably happens within hours rather than days (Dietze, Mohadjer, et al., 2017).

Precipitation is an obvious cause of slope failure, but from our data we see another aspect of water in the environment. A salient though not statistically significant feature is that cliff failures occurred more frequently during the night (Fig. 3 b). Rain has a uniform distribution throughout the day, so cannot explain this diurnal pattern of failures. During failure event days, the relative humidity values were systematically higher than during the other days in the winter and especially summer seasons (Fig. 3 b). But most importantly, cliff activity followed the daily relative humidity cycle with a time lag of 1–2 hours. Therefore, we propose that relative humidity may contribute to cliff activity at this time scale, and in the absence of rain. During the cooling hours at the end of the day, increased humidity and decreasing temperature will lead to crossing of the dew point. The condensed water can then migrate quickly into the fractured chalk at the cliff face and increase the water content in the material.

We propose that cliff failure of the type observed by us occurs primarily due to wetting of the fractured chalk, be it by rain or condensation of atmospheric moisture, causing a sharp transition in rheological behaviour of the cliff substrate (plasticity number Ip = 7.8±1.2, pers. comm. Christian Koepke, BAUGRUND Stralsund engineering office, 2019). The average water content of Rügen chalk is around 23 % (LUNG, 2019); the transition from rigid to semi-rigid occurs at 22.0±2.0 % and the transition to liquid at 29.8±2.5 % water content. Hence, the cliff material is mostly in a meta stable state, and wetting and drying cycles may cause frequent transitions between rigid and semi-rigid. Thus, rain has two complementary effects that can increase the propensity of the chalk cliff face to failure. Increased interflow contributes to failures by loading and shear strength reduction, which adds to the instantaneous effect of the material state transition at the cliff face upon sufficient wetting.

4.3 Cliff activity at the lunar cycle

The overlapping spectral peaks of cliff activity and lunar distance are unexpected. Lunar distance (JPL, 2019) affects the net local gravitational force at the Earth surface, imposing dilation of bedrock, changes in pore space and decreasing groundwater potential via tidal stress (Inkenbrandt et al., 2005). However, effects on the net gravitational force are negligible, a 10^{-7} decrease of the Earth's gravitational pull when the moon is closest to the study area. Similarly, tides in the Baltic sea are small, and sea level does not appear to have been a direct cause of detected cliff failures. An influence of the moon on groundwater has been reported, although predominantly on the diurnal and semi diurnal scale (Briciu, 2014). However, groundwater on Rügen does not show any significant lunar periodicity (Fig. 3 d). Perhaps more relevant, Cerveny et al. (2010) found a robust lunar signal in river discharge across the United States, which they attributed to a precipitation cycle synchronized with the lunar month. Our spectral data show precipitation peaks when lunar distance is greatest and cliff failures tend to happen (Fig. 3 d). Based on our data, we cannot determine the exact nature of the link between the lunar cycle and cliff coast failures on Rügen. However, all mechanisms reviewed here tend to force water availability on and within the cliff.

4.4 Biotic cliff preconditioning

There is an important seasonal effect that drives the Rügen cliff system to the level of instability that is needed for cyclic variations on shorter, lunar (Fig. 3 c) and diurnal (Fig. 3 a-b) time scales to have an effect on cliff failure. We attribute this seasonal pattern to water uptake for respiration by the dense beech forest covering the cliff hinterland. On Rügen, the vegetative season typically starts in early May and ends in October–November. In this season, water uptake by trees leads to progressive drying of the subsurface beyond the recharge capacity of summer rain events. During the subsequent season of vegetation dormancy, from November to April, water uptake is limited, and rain storms can recharge groundwater (Fig. SI 4). Hence, we infer that there is a strong vegetation control on cliff stability on Rügen, expressed on the seasonal scale. This is supported by our data on near surface seismic wave velocities (Fig. 1 e). The dv/v values of both analysed central stations were systemically high by the end of the vegetation season and stared to decline around November, before rising again in late spring. We attribute this to drying of the near-surface substrate in summer, and wetting in winter. However, this signature was not observed in groundwater levels, which fluctuated around a depth of about 15 m below the surface, suggesting that our wave velocity monitoring was sensitive to the water content near the surface. Additional effects of strengthening of the underlying chalk in summer and weakening in winter may also be comprised in bulk velocity changes. These effects have no expression in seismic wave velocities on shorter time scales.

4.5 The multi-year scale of cliff activity

We have found a months-long legacy of the climatic boundary conditions, expressed in the large number and volume of failed sites in winter 2017 after a wet summer with

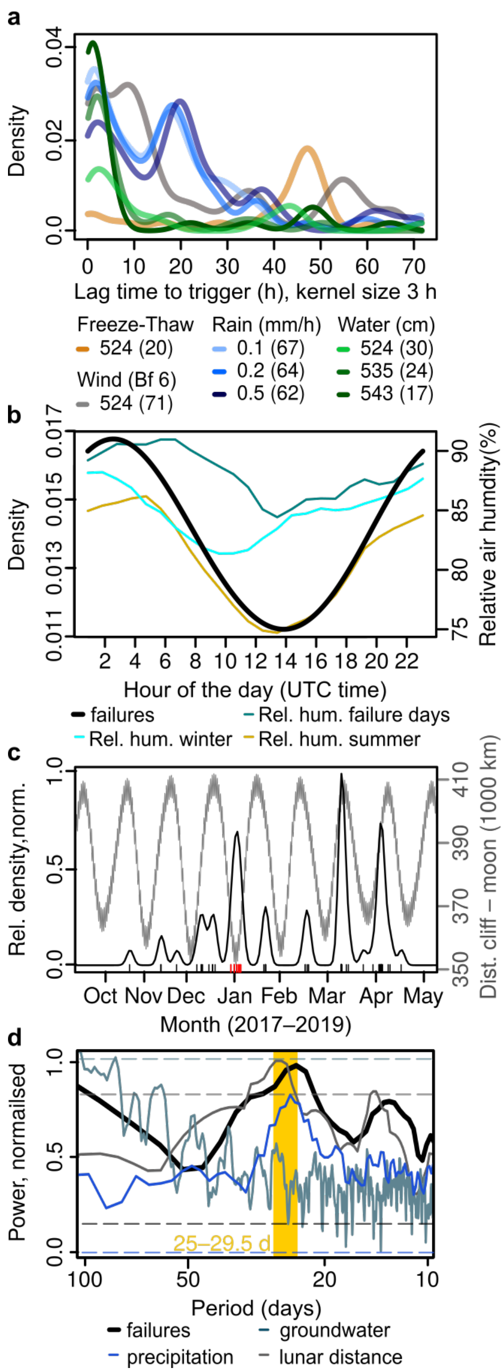

Figure 3. Drivers and triggers of cliff failures on Rügen. a) Kernel density estimates (72 h duration) of time lags between triggers and failures. Values in parentheses denote number of events within 72 h. b) Diurnal failure activity density estimate (thick black line) and relative air humidity. c) Seasonal failure density estimates (period 2017–2019). Rugs along the x axis denote individual events (red rugs indicate anomalous event around the year end 2018). Grey curve shows lunar distance, i.e., distance between the gravity centre of the moon and the cliff area. d) Spectra of cliff failures and potential drivers. Lunar distance, precipitation and failures share a common periodicity window (orange polygon) at 25.5–29 days. Horizontal dashed lines depict significance thresholds for the spectra.

126 % of average seasonal precipitation and the small failure number and volume in winter 2018, after a dry summer with only 51 % of the average precipitation.

As future climate projections for Rügen include generally drier conditions and more variable precipitation events (Frei et al., 2006; Umweltbundesamt, 2015), the chalk cliffs may experience fewer failure events as the declining groundwater input fails to drive the system to a state where rain and relative air humidity can trigger failures. This may result in a decreasing sediment supply to the near-shore environment (Stephensen, 2014), with off-site consequences, especially for adjacent sandy shorelines that may suffer from erosion due to sediment starvation. Moreover, the coast cliffs may become increasingly prone to undercutting, as the absence of a sediment apron exposes them to the direct impact of incoming waves. This may eventually lead to less frequent but more catastrophic failures as the entire cliff height will be mobilized. Unlike sandy beaches, cliffs are not able to recover after erosive events by aggradation of new material (Stephensen, 2014). Thus, there is no adjusting response mechanism in such an erosion-only system, which makes estimating the consequences of climate change for cliff coasts even more important.

5 Conclusions

In the absence of strong tidal and wave forcing, patterns and frequencies of cliff failures along the coast of Rügen, Germany, are affected by the presence of water in the cliff on a range of time scales This gives rise to distinct cycles of cliff failure at annual, seasonal, lunar and diurnal time scales. Climatic dryness/wetness sets the baseline for failure frequency, soil moisture uptake by trees suppresses failures in the vegetation period, precipitation causes events by direct rain onto and groundwater flow towards the cliff surface, and higher atmospheric moisture levels may promote failures during the night. Failure deposits are typically amalgams and the seismic approach reveals their formation as clusters of geomorphic activity rather than resulting from single events. With increasingly drier climate conditions in the future the cliff coast may grade into a transient, characterised by less frequent smaller events due to insufficient moisture preconditions, which in turn may prepare the cliff for more catastrophically large events.

Acknowledgments

The underlying data sets are provided under DOI 10.17605/OSF.IO/FV64X. The analysis scripts are provided in the supporting information. Seismic data are available via GEOFON data services. We thank Christopher Roettig and Sascha Meszner for the enlightening discussion on lunar influence on cliff activity and Björn Piltz for his input on lunar orbital parameters. An anonymous tractor driver is thanked for saving the spring 2018 survey mission.

References

Allen, R. (1982). Automatic phase pickers: Their present use and future prospects. *Bulletin of the Seismological Society of America*, *72*, S225–S242.

Briciu, A.-E. (2014). Wavelet analysis of lunar semidiurnal tidal influence on selected inland rivers across the globe. *Scientific Reports*, *4*, 4193.

Burtin, A., Hovius, N., Milodowski, D. T., Chen, Y.-G., Wu, Y.-M., Lin, C.-W., ... Leu, P.-L. (2013). Continuous catchment-scale monitoring of geomorphic processes with a 2-d seismological array. *Journal of Geophysical Research Earth Surface*, *118*, 19561974. doi: 10.1002/jgrf.20137

Cerveny, R., Svoma, B., & Vose, R. (2010). Lunar tidal influence on inland river streamflow across the conterminous united states. *Geophysical Research Letters*, *37*(L22406). doi: 1029/2010GL045564

Cook, K., & Dietze, M. (2019). Short communication: A simple workflow for robust low-cost uav-derived change detection without ground control points. *Earth Surface Dynamics*, *7*(4), 1009–1017. Retrieved from https://www.earth-surf-dynam.net/7/1009/2019/ doi: 10.5194/esurf-7-1009-2019

Dietze, M. (2018a). *'eseis' – an r software toolbox for environmental seismology. v. 0.4.0.* GFZ Data services. doi: http://doi.org/10.5880/GFZ.5.1.2018.001

Dietze, M. (2018b). The r package eseis a software toolbox for environmental seismology. *Earth Surface Dynamics*, *6*, 669-686. doi: 10.5194/esurf-6-669-2018

Dietze, M., Mohadjer, S., Turowski, J., Ehlers, T., & Hovius, N. (2017). Validity, precision and limitations of seismic rockfall monitoring. *Earth Surface Dynamics*, *2017*, 1–23. doi: 10.5194/esurf-2017-12

Dietze, M., Turowski, J. M., Cook, K. L., & Hovius, N. (2017). Spatiotemporal patterns, triggers and anatomies of seismically detected rockfalls. *Earth Surface Dynamics*, *5*(4), 757–779. Retrieved from https://www.earth-surf-dynam.net/5/757/2017/ doi: 10.5194/esurf-5-757-2017

DWD. (2019). *Climate data centre.* Retrieved from https://www.dwd.de/EN/climate_environment/cdc/cdc_node.html

Frei, C., Schöll, R., Fukutome, S., Schmidli, J., & Vidale, P. (2006). Future change of precipitation extremes in europe: Intercomparison of scenarios from regional climate models. *Journal of Geophysical Research*, *111*(D06105). doi: 10.1029/2005JD005965

GPL. (2019). *Cloudcompare, v. 2.10.1.* doi: http://www.cloudcompare.org/

Helmstetter, A., & Garambois, S. (2010). Seismic monitoring of Sechilienne rockslide (French Alps): Analysis of seismic signals and their correlation with rainfalls. *Journal of Geophysical Research*, *115*, F03016. doi: 10.1029/2009JF001532

Hibert, C., Mangeney, A., Grandjean, G., Baillard, C., Rivet, D., Shapiro, N. M., … Crawford, W. (2014). Automated identification, location, and volume estimation of rockfalls at piton de la fournaise volcano. *Journal of Geophysical Research*, *119*, 1082–1105. doi: 10.1002/2013JF002970

Hibert, C., Mangeney, A., Grandjean, G., & Shapiro, N. M. (2011). Slope instabilities in dolomieu crater, runion island: From seismic signals to rockfall characteristics. *Journal of Geophysical Research*, *116*, F04032. doi: 10.1029/2011JF002038

Inkenbrandt, P., Doss, P., Pickett, T., & Brown, R. (2005). Barometric and earthtide induced water-level changes in the inglefield sandstone in southwestern indiana. *Proceedings of the Indiana Academy of Science*, *114*, 1-8.

JPL. (2019). Retrieved from https://ssd.jpl.nasa.gov/horizons.cgi

Kennedy, D. M., Coombes, M. A., & Mottershead, D. N. (2017). The temporal and spatial scales of rocky coast geomorphology: a commentary. *Earth Surf. Process. Landforms*, *42*, 1597 1600. doi: 10.1002/esp.4150

Krienke, K., & Koepke, C. (2006). Landslides at the sea cliffs of the isle of rügen (northeast germany) during the winter of 2004/05 geology and soil mechanics. *Zeitschrift für geologische Wissenschaften*, *34*, 105-113.

Lague, B. N., D., & Leroux, J. (2013). Accurate 3d comparison of complex topography with terrestrial laser scanner: Application to the rangitikei canyon (nz). *ISPRS J. Photogramm.*, *82*, 10–26. doi: 10.1016/j.isprsjprs.2013.04.009

Letortu, P., Costa, S., Cador, J., Coinaud, C., & Cantat, O. (2015). Statistical and empirical analyses of the triggers of coastal chalk cliff failure. *Earth Surface Processes and Landforms*(40), 1371-1386. doi: 10.1002/esp.3741

Lim, M., Rosser, N., Allison, R., & Petley, D. (2010). Erosional processes in the hard rock coastal cliffs of staithes, north yorkshire. *Geomorphology*, *114*, 12–21.

LUNG. (2019). Retrieved from https://www.lung.mv-regierung.de/insite/cms/umwelt/geologie/rohstoffgeologie/rohstoffgeologie_kreidekalk.htm

Menatschi, L., Vousdoukas, M., Pekel, J.-F., Voukouvalas, E., & Feyen, L. (2018).

Global long-term observations of coastal erosion and accretion. *Scientific Reports*, *8*, 12876.

Obst, K., & Schütze, K. (2005). Analysis of cliff slides at the steep coast of jasmund, rügen in 2005. *Zeitschrift für geologische Wissenschaften*, *34*, 11-37.

Sens-Schönfelder, C. (2014). *Monitoring and imaging based on interferometric concepts package.* Retrieved from `https://github.com/miic-sw/miic`

Sens-Schönfelder, C., & Wegler, U. (2006). Passive image interferometry and seasonal variations of seismic velocities at merapi volcano, indonesia. *Geophysical Research Letters*, *33*(21).

STALUVP. (2019). *Groundwater log time series, buddenhagen, rügen.*

Stephensen, W. (2014). Rock coasts. In D. Masselink & R. Gehrels (Eds.), *Coastal environments and global change* (first edition ed., p. 256-379). John Wiley & Sons.

Stock, G., Collins, B., Santaniello, D., Zimmer, V., Wieczorek, G., & Snyder, J. (2013). Historical rock falls in yosemite national park. *U.S. Geological Survey Data Series 746*, *746*, 17.

Umweltbundesamt. (2015). *Germany's vulnerability to climate change.* Retrieved from `https://www.umweltbundesamt.de/sites/default/files/medien/378/publikationen/climate_change_24_2015_summary_vulnerabilitaet_deutschlands_gegenueber_dem_klimawandel_2.pdf`

Vann Jones, V., Rosser, N., Brain, M., & Petley, D. (2015). Quantifying the environmental controls on erosion of a hard rock cliff. *Marine Geology*, *363*, 230–242. doi: 10.1016/j.margeo.2014.12.008

Wieczorek, G. (1996). Landslide triggering mechanisms. In A. Turner & R. Schuster (Eds.), *Landslides–investigation and mitigation* (pp. 76–90). Transportation Research Board, National Research Council, National Academy Press.

WSV. (2019). Retrieved from `http://www.pegelonline.wsv.de`

Young, A., & Carilli, J. (2019). Global distribution of coastal cliffs. *Earth Surface Processes and Landforms*, *44*, 1309–1316.